RSC Advances

ROYAL SOCIETY OF CHEMISTRY

PAPER

View Article Online
View Journal | View Issue

Check for updates

Cite this: *RSC Adv.*, 2020, **10**, 41532

Open Access Article. Published on 13 November 2020. Downloaded on 2/25/2026 10:59:45 AM.
This article is licensed under a Creative Commons Attribution-NonCommercial 3.0 Unported Licence.

N,S co-doped hierarchical porous carbon from Chinese herbal residues for high-performance supercapacitors and oxygen reduction reaction†

Lin Zhang,[a] Qinqin Xu,*[a] Xia Wang,[a] Qi Sun,[a] Feng He,[a] Weidong Pan[b] and Haibo Xie *[a]

Received 6th August 2020
Accepted 6th November 2020

DOI: 10.1039/d0ra06780f

rsc.li/rsc-advances

The sustainable development of human society is facing challenges of resource depletion, energy crisis and worsening environment. In this work, a typical Chinese herbal residue (gallnut residues), with a large amount of organic waste threatening the environment after extracting the bioactive components, especially in China, was used as a single precursor for both a carbon and heteroatoms source to prepare heteroatoms co-doped hierarchical porous carbon *via* carbonization and a subsequent KOH activation. The prepared nitrogen, oxygen and sulfur co-doped porous carbons (NOSPC-*X*) show developed hierarchical micro–mesoporous structures, high specific surface areas, as well as high content of N/S co-doping. When used as supercapacitor electrodes, NOSPC-800 exhibits excellent electrochemical performance with an ultrahigh specific capacitance, a high energy density of 11.25 W h kg^{-1} at 25 W kg^{-1} and an excellent charge–discharge cycling stability of 96.5% capacitance remained after 10 000 cycles. As an ORR electrocatalyst, it shows outstanding ORR activity as well as much better stability and methanol-tolerance capacity than that of a commercial Pt/C catalyst. The unique hierarchical micro–mesoporous architecture, high surface area as well as optimal N and S co-doping level make biomass-derived NOSPC-800 an excellent candidate for electrode materials in diverse electrochemical energy applications.

Introduction

The sustainable development of human society is facing challenges of resource depletion, energy crisis and environment worsening.[1,2] It is well accepted that the development of energy, materials, and chemicals from renewable resources *via* sustainable technologies can significantly contribute to the solution of these challenges. Therefore, a considerable sustainable energy conversion and storage devices are urgently needed to resolve the current problems.[3,4] Supercapacitors (SCs) and fuel cells (FCs) are two promising energy-storage devices that have aroused worldwide research in the past few decades.[5–7] Currently, SCs suffer from low energy densities, specific capacitance and rate performance due to an inappropriate porous structure.[8] It is well known that carbon materials with hierarchical pore size distribution are critical to obtain good energy storage characteristics,[9,10] of which macropores can serve as the ion-buffering reservoirs in the interior of carbon materials, mesopores can be as channels to accelerate the rapid transport of ions, and micropores can work as the active sites for charge accommodation.[11] Hierarchically structural carbon materials also present great potential in FCs as the carbon materials are promising alternatives to substitute high cost Pt-based noble metals electrodes and boost ORR,[12–14] in which hierarchically porous structure can prompt mass transport and yield abundant accessible active sites.[15–17] Actually, the targets of the structure and component features for ideal supercapacitor electrode materials and metal-free ORR catalysts are consistent.

The surface functionalization of carbon materials also plays a key role in improving their electrochemical properties. Heteroatom doping (*e.g.* N, S, P, O *etc.*) can effectively regulate the morphology, structure and electronic properties of carbon materials, so as to meet more application requirements, such as effectively improving the capacitance and catalytic properties of porous carbon materials.[18,19] Post-treatment and *in situ* doping are two common nitrogen doping methods. Among them, the post-treatment method is to introduce the heteroatoms containing precursor into the synthesized carbon materials combined with other treatments such as templating or carbonization. However, it suffers from the problems including complicated synthesis steps, low doping amount, uncontrollable and uneven heteroatoms doping.[20,21] *In situ* doping can

---

[a] *Department of New Energy Materials & Engineering, College of Materials & Metallurgy, Guizhou University, Huaxi District, Guiyang 550025, P. R. China. E-mail: qqxu1@gzu.edu.cn*

[b] *State Key Laboratory of Functions and Applications of Medicinal Plants, Guizhou Medical University, 3491 Baijin Road, Guiyang 550014, PR China*

† Electronic supplementary information (ESI) available. See DOI: 10.1039/d0ra06780f

This journal is © The Royal Society of Chemistry 2020

Open Access Article. Published on 13 November 2020. Downloaded on 2/25/2026 10:59:45 AM.
This article is licensed under a Creative Commons Attribution-NonCommercial 3.0 Unported Licence.

effectively regulate the hierarchical structure and electrochemical properties of carbon materials by simply adjusting the source structure of heteroatoms-containing precursors and the adding methods.[22] Thus, the development of simple and efficient methods to prepare hierarchically porous structure and heteroatom doped carbon is highly attractive. For this purpose, biomass becomes a source of attractive precursors, due to their intrinsic composition and natural structural features.[23] Its well-connected micro-structure and multichannel structure for water and minerals, can be viewed as the self-template to produce hierarchical porous structure of carbon materials.[24] Moreover, biomass is rich in various basic elements such as C, N, S, P, and so on. Therefore, it can be reasonably predicted that the *in situ* and self-doped carbon materials can be prepared by pyrolysis and carbonization of biomass.[25] Due to the advantages of homogenous heteroatom distribution, appropriate pore distribution and controlled dopant content in the resultant carbons, the biomass-based carbon is expected to be a promising carbon electrodes candidate.[26] Moreover, the biomass-based carbon is generally cheap, environmentally friendly, accessible, and recyclable as well as extensively available.[27] In recent years, researchers have paid increasing attention to employing green, reproducible biomass or its derivatives, and renewable materials to prepare heteroatoms-doped hierarchical porous carbons, such as cornstalk,[28] garlic skin,[29] ant powder,[23] wheat flour,[10] *etc.*, which not only greatly reduce the cost, but also inherit both the structural flexibility and chemical diversity of the natural resources.

Chinese herbal has played an important role in the world medical system, especially in Chinese communities. With the enforcement of modernization of traditional Chinese medicine, plenty of Chinese herbal-derived organic waste was produced after extracting the bioactive components every year, and it has been up to 3×10^7 tons per year in recent years.[30] Chinese herbal-derived organic waste usually has an unpleasant smell, high water content, and their direct discarding has caused serial environmental pollution, such as atmospheric pollution, water pollution as well as soil pollution, which has been regarded as an emerging industrial solid waste in China. The Chinese herbal residue is mainly composed of lignocellusic biomass, fatty, starch, protein and so on.[31] In order to solve the waste problem, the residues have been tried to be used as resources for biological fertilizer, poultry feed through complex post-pretreatment processes, and so on. However, the current disposal strategies still cannot meet the increasing production of Chinese herbal-derived organic waste. Therefore, the exploration of new potential use of this waste is prime both from the points of view of resources utilization and environment protection. Chinese gallnut (also called Wubeizi) is a kind of forest by-product and is used as a common Chinese herbal medicine, with tannic acid as the main active ingredient. Being a typical Chinese herbal residue, gallnut residues are consisted of a shell of plants and a core of gall, which is rich in a variety of heteroatom elements such as C, N, S, O, *etc.* Therefore, it is likely to be a good precursor for multiple heteroatom doped carbon materials.

Herein, in this work, we present a facile approach to prepare N/S co-doped porous carbon materials by using Chinese herbal residues (gallnut residue) as the only source *via in situ* self-doping. A series of N/S co-doped porous carbon materials (NOSPC-*X*) with ultrahigh surface area up to 3351.8 $m^2\ g^{-1}$ as well as moderate nitrogen content (2.73 at%) and sulfur content (0.28 at%) were prepared *via* carbonization and KOH activation. The electrochemical properties were systematically studied when it was used as electrodes in SCs and FCs. The study presents an example of high-value-added use of Chinese herbal-derived organic waste, and discovers the value of this zero-cost of solid waste resources.

Experimental

Materials synthesis

Chinese gallnut residues were collected from the local company, washed by ultrapure water, dried at 60 °C for 12 h, and then ground into powder with a mortar. The dried Chinese gallnut residue powders were pre-carbonized with a heating rate of 5 °C min^{-1} heated to 300 °C and kept for 1 h in a horizontal tubular furnace in an Ar atmosphere. Subsequently, the pre-carbonized powders were ground and mixed with KOH at a weight ratio of 1 : 4. Then the solid mixtures were transferred into a nickel boat, firstly heated to and maintained at 300 °C for 1 h and then heated to 700 °C, 800 °C and 900 °C, respectively, for 2 h in a tube furnace for carbonization under Ar atmosphere. After cooling down to room temperature, the obtained samples were washed with 1 M HCl and ultrapure water several times until the pH = 7. Finally, the samples were dried at 80 °C in vacuum overnight, and labeled as NOSPC-*X* (*X* is the temperature of carbonization). For comparison, the carbon material from Chinese gallnut residues with the same procedure as that of NOSPC-800 without KOH activation was also prepared and named as NOSC-800.

Materials characterization

The morphologies and structures of the samples were characterized by transmission electron microscopy (TEM, Tecnai G2 F20), X-ray diffraction (PXRD, Panalytical, X'PertPowder, Cu Kα radiation), Raman spectrometry (Horiba Scientific LabRAM HR Evolution, under excitation at 532 nm), and X-ray photoelectron spectroscopy (XPS, ESCALAB 250Xi, Thermo Fisher, USA, using Al Kα radiation as the excitation source). Element analysis (EA) (Elementarvario el cube) was employed to get elemental compositions. To investigate the specific surface area (SSA) and pore size distribution (PSD) of the samples, N_2 adsorption–desorption measurements were performed on a Micromeritics Instrument 3Flex at 77 K after being vacuum-dried at 300 °C for 12 h. The SSA was calculated using the Brunauer–Emmett–Teller (BET) method, and the PSD was calculated by the Non-Local Density Functional Theory (NLDFT) model.

Electrochemical characterization

The supercapacitor performance of the carbon materials was carried out in a two-electrode system by assembling a CR2032

Open Access Article. Published on 13 November 2020. Downloaded on 2/25/2026 10:59:45 AM.
This article is licensed under a Creative Commons Attribution-NonCommercial 3.0 Unported Licence.

coin-type cell. The working electrodes were prepared by coating the mixture of PTFE (10 wt%), acetylene black (10 wt%) and the active material (80 wt%) on nickel foam (diameter 1 cm), then dried at 80 °C for 12 h. Compressed by a tablet machine at 5 MPa for 2 min, the nickel foam disk was washed by ethanol, and finally dried at 60 °C for 4 h. A polypropylene membrane was used as the separator and 6 mol L^{-1} KOH was used as the electrolyte. The mass loading of active materials in each working electrode is 3–4 mg cm^{-2}. After assembly, the working electrodes were characterized by cyclic voltammetry (CV), galvanostatic charge–discharge (GCD) and electrochemical impedance spectroscopy (EIS) on a CS2350 electrochemical work-station (Wuhan Corrtest Instruments Corp., Ltd, China).

The specific capacitances of SCs were examined by the GCD measurements, at the current densities of 0.1, 0.5, 1, 2, 4, 10 and 20 A g^{-1}, respectively, with the potential ranging from 0 to 1 V. For the CV measurements, the sweep rates were 5, 10, 20, 50, 100, 200 mV s^{-1}, respectively, with the potential ranging from 0 to 1 V. For the EIS measurements, the frequency range was from 10 mHz to 100 kHz. The specific capacitance Cs (F g^{-1}) examined by the GCD was calculated based on the following equation (eqn (1)):

$$C_s = \frac{2I\Delta t}{m\Delta V} \tag{1}$$

where m (g) is the mass of the active material on a single working electrode, I (A) is the constant discharge current, Δt (s) is the discharging time, and ΔV (V) is the potential window.

The energy density (E) and power density (P) were calculated based on the following eqn (2) and (3):

$$E = \frac{1}{2 \times 4 \times 3.6} C\Delta V^2 \tag{2}$$

$$P = \frac{3600E}{\Delta t} \tag{3}$$

where E (W h kg^{-1}) and P (W kg^{-1}) are energy and power density, respectively, Δt (s) is the discharging time, C represents the specific capacitance and ΔV (V) is the potential window.

The ORR electrocatalytic properties were estimated by rotating disk electrode (RDE) measurements in a conventional three-electrode cell on CS2350 electrochemical work-station (Wuhan Corrtest Instruments Corp., Ltd, China) at room temperature, that rotating disk electrode was consisted of a glassy carbon electrode and the as-prepared catalyst ink. A Pt wire as counter electrode and a Hg/HgO electrode as reference electrode (0.098 V relative to the reversible hydrogen electrode, RHE). The electrolyte was N_2/O_2-saturated 0.1 M KOH solution. The CVs were tested from −0.8 to 0.4 V with a scan rate of 10 mV s^{-1}. Specially, the linear sweep voltammograms (LSVs) curves were recorded with a scan rate of 5 mV s^{-1} under different electrode rotation rates (400, 625, 900, 1225, 1600, 2025 and 2500 rpm) by rotating disk electrode (RDE) measurement. The values (n) of electron-transfer number by the rotation disk electrode (RDE) measurement was according to the following eqn (4):

$$\frac{1}{J} = \frac{1}{J_0} + \frac{1}{J_K} = \frac{1}{B\omega^{0.5}} + \frac{1}{J_K} \tag{4}$$

where J is the measured current density of catalyst, J_0 is the diffusion limiting current density, J_K is the kinetic-limiting current density, ω is the electrode rotating rate. B is obtained from the slope of K–L plot (eqn (5)):

$$B = 0.2nFC_0(D_0)^{2/3}\nu^{-1/6} \tag{5}$$

The constant 0.2 is adopted when the rotation rate is expressed in rpm, n is the number of electron transfer per O_2 molecule, F is the Faraday constant ($F = 96\ 485$ C mol^{-1}), C_0 and D_0 are the bulk concentration (1.2×10^{-3} mol L^{-1}) and diffusion coefficient (1.9×10^{-5} cm^2 s^{-1}) of O_2 in 0.1 mol L^{-1} KOH solution, respectively, and ν is the kinematic viscosity of 0.1 mol L^{-1} KOH solution.

The working electrode ink was prepared by ultrasonically dispersing 10 mg of the carbon material and 100 μL of 5% Nafion suspension in 1.8 mL solution containing ethanol and deionized water, 5 : 1 by volume or 2 h to get a uniform ink. Before RDE experiments, 15 μL of the solution was carefully applied to the 0.196 cm^2 disk, and then dried at room temperature for the rotation disk electrode (RDE) measurement. The commercial Pt/C (20 wt%) electrodes were prepared in the same way for comparison.

Results and discussion

Material characterization

The microstructures of the prepared samples were characterized by TEM. Fig. 1 shows TEM and HRTEM images of NOSC-800 and NOSPC-Xs samples. It can be seen from Fig. 1(a) that there are almost no micropores and mesopores in NOSC-800 (without KOH activation), while NOSPC-Xs (with KOH

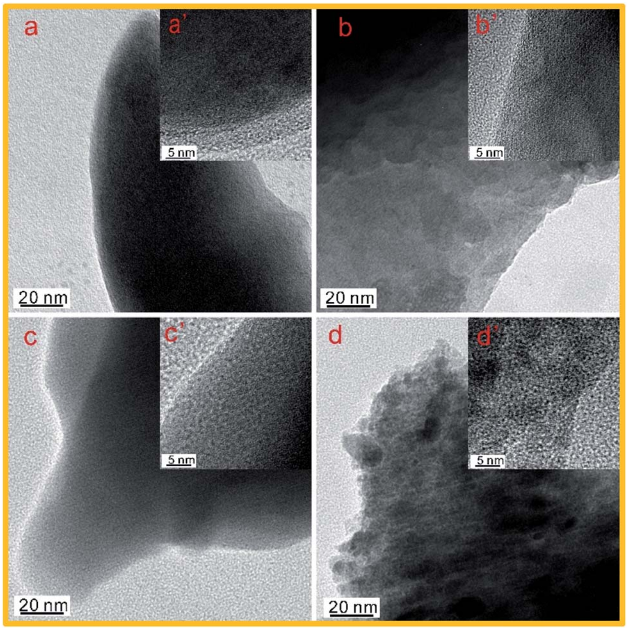

Fig. 1 TEM and the corresponding HRTEM images of (a) and (a′): NOSC-800, (b) and (b′): NOSPC-700, (c) and (c′): NOSPC-800 and (d) and(d′): NOSPC-900 carbon samples.

Open Access Article. Published on 13 November 2020. Downloaded on 2/25/2026 10:59:45 AM. This article is licensed under a Creative Commons Attribution-NonCommercial 3.0 Unported Licence.

activation) have abundant mesopores and microporous structures that cross each other (Fig. 1b–d), which can be mainly attributed to the activation of KOH, that the reaction between KOH and carbon produces pores and facilitates pore formation at high temperatures. For supercapacitors, the extensive existence of abundant mesopores and micropores can not only provide more active sites, but also provide convenient and continuous channels for the smooth entry and transfer of electrolyte ions and mass, such that these porous structures are beneficial for enhancing the electrochemical performance.[32] Meanwhile, it can be observed from the HRTEM images in Fig. 1b′–d′ that all NOSPC-*X* samples have micropores with a diameter of 1–5 nm and exhibit wormlike shape, which is the feature of carbon materials with well-organized micropore and mesopore structure, also indicating a large specific surface area of the carbon materials.[27]

The porous structure and specific surface areas of as-prepared carbon materials were calculated by N_2 adsorption–desorption measurements. Fig. 2(a) displays the N_2 adsorption–desorption isotherms of all the samples. NOSC-800 prepared by direct carbonization has no apparent uptake of N_2, implying its non-porous structure. However, the NOSPC-700 presents a type I isotherm characteristic with a drastic increase in the adsorbed volume at low relative pressures (P/P_0 < 0.1) and the weak hysteresis loops at high relative pressure, indicating the presence of micropores and a small amount of mesopores. The NOSPC-800 and NOSPC-900 show similar isotherms which are consisted of type I and type IV isotherm indicating the hierarchical porous structure of two samples. In detail, a sharply increasing adsorption capacity at low relative pressure (P/P_0 at low relative pressure $P/P_0 < 0.1$) was observed, suggesting a large proportion of micropores in the samples. Furthermore, a type IV hysteresis loop caused by capillary condensation at relative pressure P/P_0 ranging from 0.5 to 1 was observed, which implied the existence of mesopores in NOSPC-800 and NOSPC-900.[6,11,33] The pore size distribution curves (Fig. 2(b)) reveal the micro- and mesoporous structure of NOSPC-*X*s, derived from the release of small molecule volatile products due to decomposition of carbon and the KOH activation.[8] The results are consistent with the TEM observation shown in Fig. 1. Furthermore, the porous properties of the samples are summarized in Table 1. The BET surface areas of NOSC-800 and NOSPC-800 are calculated to be 19.2 m^2 g^{-1} and 3351.8 m^2 g^{-1}, respectively, which clearly indicates that the use of KOH significantly enhances the SSA of the samples. Except for the influence of KOH, the carbonization temperature has an important role on the pore structure formation of NOSPC-*X*s. With the increase of temperature from 700 °C to 800 °C, the surface area increases from 2000.8 m^2 g^{-1} (NOSPC-700) to 3351.8 m^2 g^{-1} (NOSPC-800), and the pore volume increases from 0.97 to 2.16 cm^3 g^{-1} correspondingly. However, activation at higher temperature (above 800 °C) will lead to severe collapse of partial structural, resulting in mesopore consolidation or enlargement, thus reducing the surface area to 3179.3 m^2 g^{-1} (NOSPC-900). By providing an effective access of the electrolyte ions into the contact sites, the hierarchical porous structure can facilitate the ion transport and minimize the high-rate diffusional loss.[16,34] Hence, compared to NOSC-800, NOSPC-700, NOSPC-800 and NOSPC-900, the NOSPC-800 sample with high surface area is expected to illustrate higher performance both in the SC and electrocatalytic ORR.

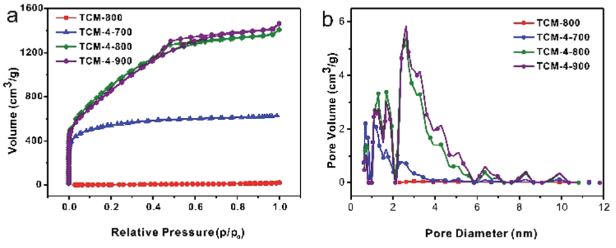

Fig. 2 (a) N_2 adsorption–desorption isotherms, (b) pore size distribution (PSD) profiles of NOSC-800 and NOSPC-*X* samples.

PXRD and Raman spectroscopy were carried out to further understand the internal structure of the carbon samples (Fig. 3(a)). There are two obvious diffraction peaks at 25° and 43° on the samples NOSC-800 and NOSPC-700, corresponding to (002) and (100) crystal faces of carbon, respectively, indicating the existence of crystalline graphite in both samples.[28] However, both the two characteristic peaks on NOSPC-800 and NOSPC-900 are very weak (Fig. S1†), due to the reason that the activation of KOH increases the defects of the materials and thus reduces the intensity of diffraction peaks. Fig. 3(b) shows the Raman spectra of NOSC-800 and NOSPC-*X* samples, which can help study the degree of graphitization of the samples. The D-band represents the defects and disorder structure (1350 cm^{-1}) inside the carbon material, and the G-band reflects the bond stretching of sp^2 hybridization of the carbon material (1580 cm^{-1}), and the intensity ratio between the D-band strength and the G-band strength (I_D/I_G) represents the degree of graphitization inside the carbon material.[35] The I_D/I_G ratios are 1.05, 1.36 and 1.15 for NOSPC-700, NOSPC-800 and NOSPC-900, respectively, with the highest I_D/I_G value for NOSPC-800, demonstrating that there are more defects generated on NOSPC-800 carbon sample. Noteworthy, the I_D/I_G ratio of NOSPC-700 (1.05) is even lower than that of NOSPC-800 (1.36), which may be due to the incomplete activation of KOH at 700 °C, suggesting that both high temperature and KOH activation have great influences on the graphitization degree of carbon materials.

To understand the role of heteroatoms functionalities in electrochemical performance, it is necessary to clarify the types of heteroatoms doped into the carbon materials *via* XPS (Fig. 4) and calculate the content of heteroatoms by EA (Table S1†). From the wide-scan XPS spectra of NOSC-800 and NOSPC-*X* samples (Fig. 4(a)), there are four characteristic peaks are observed at ∼173 eV, ∼284 eV, ∼405 eV and ∼532 eV, respectively, indicating four elements of S, C, N and O present on the prepared samples.[34] The results indicate that N and S are successfully doped into the hierarchical porous carbon. As illustrated in Fig. 4(b), the high-resolution O1s spectrum can be divided into three individual peaks C=O (O-I: 531.9 eV), C–O (O-II: 532.5 eV), and –COOR (O-III: 533.7 eV).[25] The main effects of oxygen functional groups are increasing the conductivity by

Open Access Article. Published on 13 November 2020. Downloaded on 2/25/2026 10:59:45 AM.
This article is licensed under a Creative Commons Attribution-NonCommercial 3.0 Unported Licence.

Table 1 Physicochemical properties of the NOSC-800 and NOSPC-*X* samples

Samples	$S_{BET}{}^{a}$ (m^2 g^{-1})	$V_{total}{}^{b}$ (cm^3 g^{-1})	$V_{micro}{}^{c}$ (cm^3 g^{-1})	D^{d} (nm)
NOSC-800	19.2	0.03	0.007	4.08
NOSPC-700	2000.8	0.97	0.456	2.18
NOSPC-800	3351.8	2.16	0.273	2.38
NOSPC-900	3179.3	2.24	0.259	2.50

[a] Specific surface area. [b] The total pore volume. [c] The micropores volume. [d] The most probable size of pore.

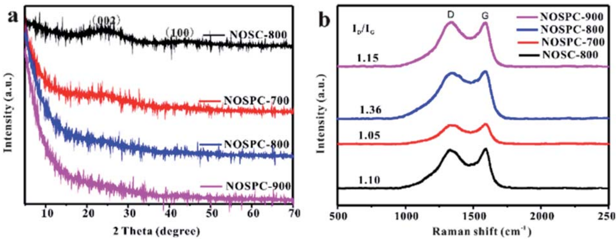

Fig. 3 (a) PXRD patterns and (b)Raman spectra of NOSC-800 and NOSPC-*X* samples.

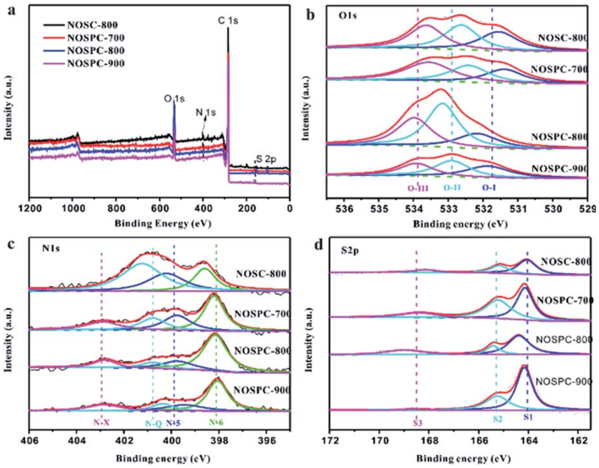

Fig. 4 (a) Wide-scan XPS spectra of NOSC-800 and NOSPC-*X*; High-resolution (b)O1s, (c)N1s, (d) S2p spectra of NOSC-800 and NOSPC-*X* samples.

improving the wettability of carbon materials in SCs and promoting the ability of adsorbing O_2 to reducing the over-potential of ORR. Similarly, the high-resolution N1s spectrum (Fig. 4(c)) are deconvoluted into four peaks which are corresponding to pyridinic N (N-6: 398.6 eV), pyrrolic N (N-5: 400.2 eV), graphitic N (N-Q: 401.2 eV) and oxidized-N (N-Q: 402.8 eV).[27,36,37] Pyridinic nitrogen and pyrrolic nitrogen are two major chemical states of N atom, which can increase the active sites and defects of materials, thus promoting the storage capacity of materials by introducing pseudocapacitance, and these N chemical states can also act as the active sites for ORR.[38] Meanwhile, graphitic N could improve the conductivity of electrode materials which can increase the rate performance of SC and the active performance of ORR. The high-resolution S2p spectrum (Fig. 4(d)) reveals three deconvoluted peaks, where the two centered at ~164.3 eV and ~165.4 eV are attributable to C–S bonding and one centered at 168.8 eV is assigned to an oxidized sulfur moiety ($-SO^{n-}$).[23] The doping of S atom could increase the activity sites by inducing defect owning to the large atomic radius of S, which can effectively enhance the storage capacity and improve ORR kinetics. In addition, the surface containing nitrogen, oxygen and sulfur functional groups can improve the wettability, reduce the resistance and improve the electrochemical efficiency. These properties may have endowed the product significant potential as a high-performance electrode material for supercapacitor and oxygen reduction reaction, which will be discussed *vide infra*. The detailed elemental percentages of S, C, N and O in NOSC-800, NOSPC-700, NOSPC-800 and NOSPC-900 samples were measured by EA as shown in Table S1.† It can be observed that with carbonization temperature increasing, both the O and N contents decrease, and the C content increases, which is due to the N/O decomposition from carbon lattice and the pyrolysis of surface C–N and C–O bonds with the increasing temperature, thereby leading to elimination and/or stabilization of sp^3 saturated oxygen-containing groups and the restoration of the sp^2 conjugated graphene basal plane of the structures.[39,40] The S content of NOSPC samples increase a lot compared to that of NOSC (before KOH activation), which can be attributed to the much slower decomposition of S, due to the higher bond energies of the S–O and S=O covalent bonds over that of C–N or C–C covalent bonds.[26,41,42] In general, the content of S element keeps relatively steady from 700–900 °C.

Supercapacitor performance

The electrochemical performance of the materials was characterized by CV, GCD and EIS tests in the electrolyte of 6 M KOH. Fig. 5(a) shows the cyclic voltammetry measurements of the samples at the scanning rate of 50 mV s^{-1} under a voltage window of 0 to 1 V. The CV curves of the samples all present quasi-rectangular shapes, indicating that they have the combination effects of electric double-layer capacitance and pseudo-capacitance, the latter of which could be attributed to the faradaic reactions associated with the heteroatoms doped in the structure. Of all the CVs, the area of the NOSPC-800 sample is the largest, indicating that the carbon material has the largest capacitance. Fig. 5(b) shows the GCD curves at the current density of 0.1 A g^{-1}, all carbon materials present a quasi-isosceles triangular shape, which indicates that the material has pseudo-capacitance characteristics. Based on the GCD measurements, the specific capacitances are calculated to be

Open Access Article. Published on 13 November 2020. Downloaded on 2/25/2026 10:59:45 AM.
This article is licensed under a Creative Commons Attribution-NonCommercial 3.0 Unported Licence.

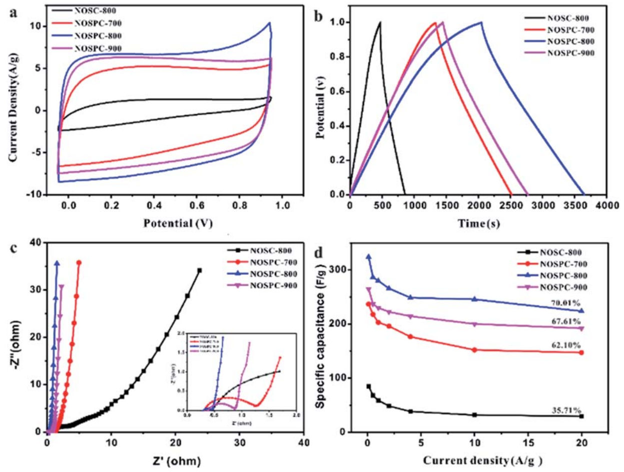

Fig. 5 Electrochemical performance of NOSC-800 and NOSPC-*X* measured in a two-electrode system in 6 mol L^{-1} KOH, (a) CV curves at 50 mV s^{-1}; (b) GCD curves at 0.1 A g^{-1}; (c) EIS spectra (Nyquist plots) (inset shows the locally enlarged Nyquist plots in the high frequency region); (d) the relationship between specific capacitance and current density.

84.2, 236.72, 324.06 and 265.04 F g^{-1} for NOSC-800, NOSPC-700, NOSPC-800 and NOSPC-900, respectively, with the NOSPC-800 sample exhibiting the largest specific capacitance, which agrees with the result obtained from the CV tests. Fig. 5(c) shows the Nyquist impedance spectra of all the samples in a frequency range of 10 kHz to 10 MHz in a 6 M KOH electrolyte. The Nyquist curves of NOSPC-*X* samples in the low frequency region are almost vertical, exhibiting the ideal capacitance performance. However, in the low frequency region, the curve of 45° appears in the NOSC-800, which indicates that the capacitance performance of the material is very poor. The intercept of the solid line in the high frequency region can be obtained from the enlarged picture of the high frequency region, which is the value of the equivalent series resistance (ESR). All NOSPC-*X*s samples show a very small value less than 0.5 Ω, which shows a good conductivity. The semicircle diameter reflects the charge transfer resistance at the interface between the electrolyte and the electrode, and a smaller semicircle indicates a higher conductivity level of the electrode. It can be observed that NOSPC-800 has a very small equivalent series resistance and charge transfer resistance, and has a good conductivity in the aqueous electrolyte. The superior electrochemical performance of NOSPC-800 could be ascribed to the hierarchical porous structure which minimizes the transport resistance of electrolyte ions. It is believed that very low ESR is crucial for enhancing both the rate capability and the power density of the electrochemical supercapacitors. Fig. 5(d) shows the capacitance retention performances of the samples. With a largest specific capacitance and over 70% capacitance retention, NOSPC-800 exhibits a good capacitance retention capability.

The electrochemical supercapacitance performance of NOSPC-800 was further studied in a two-electrode system with 6 M KOH as electrolyte under a voltage window of 0–1.0 V (Fig. 6). As shown in Fig. 6(a), the CV curves at different scanning rates all present the quasi-rectangular shape, indicating that the material has good capacitance performance. Fig. 6(b) shows the GCD curves of NOSPC-800 at different current densities, with a high specific capacitance up to 324.06 F g^{-1} obtained at the current density of 0.1 A g^{-1}. In addition, the NOSPC-800 material also shows an excellent cycle stability (Fig. 6(c)). After 10 000 times of constant current charge and discharge tests at 4 A g^{-1}, its specific capacitance still maintains 96.5%, which illustrates that the NOSPC-800 sample displays an outstanding long-term cycling durability as the carbon electrode. Fig. 6(d) displays the Ragone plot of NOSPC-800 in 6 M KOH, a maximum energy density of 11.25 W h kg^{-1} was achieved at the power density of 25 W kg^{-1}. Moreover, the energy density of NOSPC-800 remains 7.77 W h kg^{-1} when power density reaches 5000 W kg^{-1}, suggesting an excellent application prospect for NOSPC-800. The electrochemical performance of the carbon sample in this work and other samples derived from various biomass precursors are compared in Table S2,† and it can be observed that the carbon sample NOSPC-800 prepared in this work exhibits superior supercapacitance performance, indicating a bright application prospect in supercapacitors.

The gravimetric specific capacitance, the total surface content of N, O and S, and the content elements of the surface N, O and S configurations of the carbon samples are calculated so as to identify the correlation between the surface elemental compositions, SSA and their electrochemical performance of the as-prepared carbon materials (Fig. 7 and Table 2). As shown in Fig. 7(a), that carbon materials exhibit satisfactory specific capacitance (>200 F g^{-1}) with the SSA over ~2000 m^2 g^{-1}, indicating that SSA plays a vital part in the materials' specific capacitance. Additionally, this consequence not only illustrated that the high SSA could provide abundant sites to adsorb electrolyte ions on the electrode surface but also proved that the proper pore distribution is conducive for both the

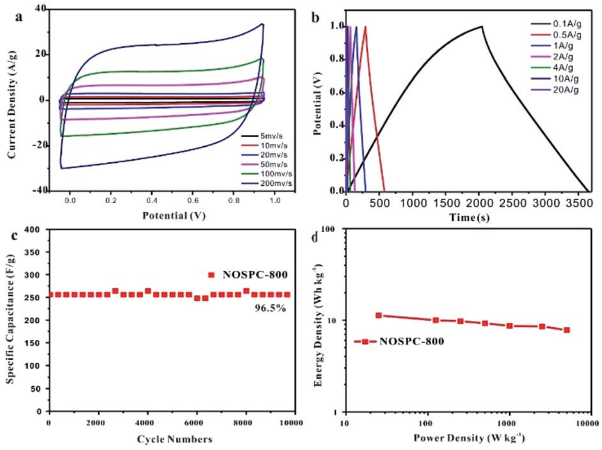

Fig. 6 Electrochemical performance characteristics of NOSPC-800 measured in a two-electrode system in the 6 mol L^{-1} KOH electrolyte. (a) CV curves at different scan rates; (b) GCD curves at different current densities; (c) cycling stability at a current density of 4 A g^{-1}; (d) Ragone plot.

Open Access Article. Published on 13 November 2020. Downloaded on 2/25/2026 10:59:45 AM. This article is licensed under a Creative Commons Attribution-NonCommercial 3.0 Unported Licence.

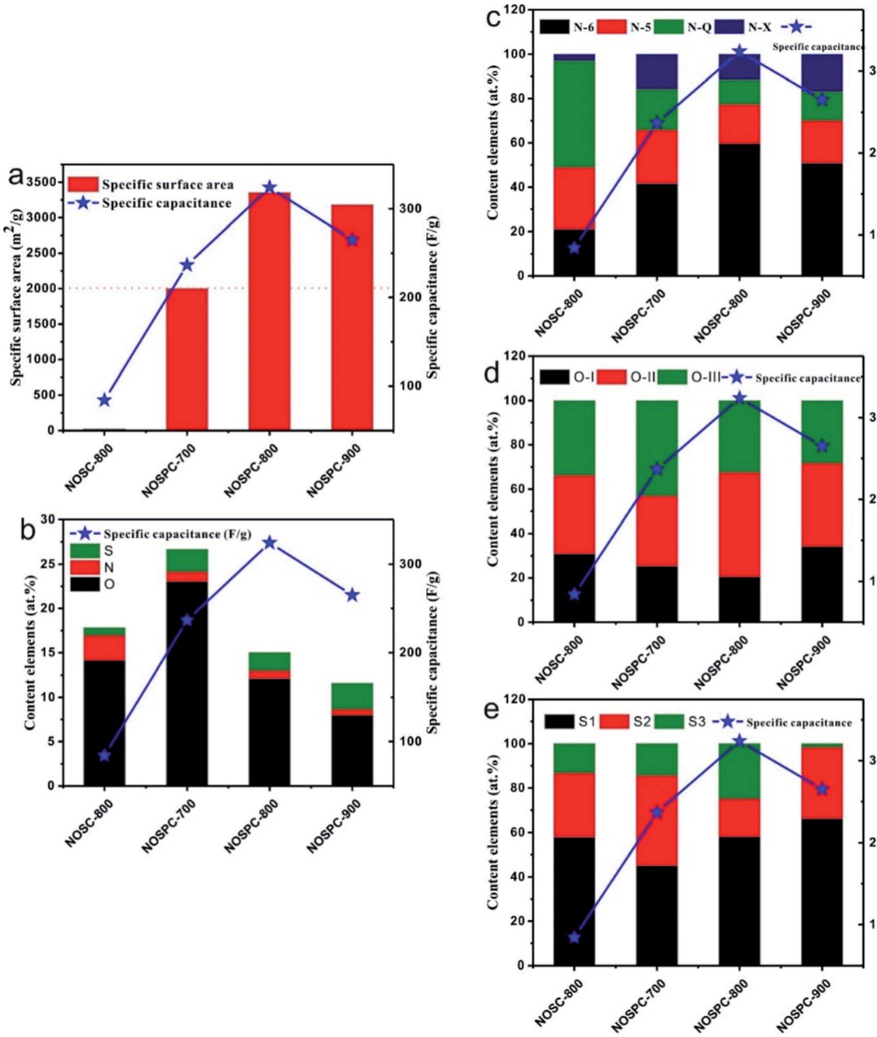

Fig. 7 (a) Gravimetric specific capacitance and specific surface area, (b) content of elements N, O, S and specific capacitance, (c) the content of surface N configuration and specific capacitance, (d) the content of surface O configuration and specific capacitance, (e) the content of surface S configuration and specific capacitance, of the preparedNOSC-800 and NOSPC-*X* carbon material samples.

storage and transport of electrolyte ions, which contributes to a large electrical double layer capacitance.[15] It can be found that there is no apparent relationship between the total content elements (N, S, O) and the specific capacitance from Fig. 7(b). Actually, a proper N chemical state distribution in N-5, N-6, N-Q, and N-X, a moderate O chemical state distribution in O-I, O-II, and O-III, and a good S chemical state distribution in S1, S2 and S3 (Fig. 7(c)–(e)) is another desirable structural feature which can lead to superior electrochemical properties. It is worth noting that the specific capacitance is positively promoted with the element contents of N-6, O-II, and the total content of S1 and S3, indicating that these three element configurations are conducive to the increase of specific capacitance. In general, it is believed that N-6 can help to reduce the resistance of the ions transfer and thus result in the increase of pseudocapacitance.[22,40] On the other hand, O-II can help to improve the wettability of these carbon materials, producing a hydrophilic surface, and bring in pseudocapacitance by redox

Table 2 N, O, S contents evaluated from XPS of NOSC-800 and NOSPC-*X* samples

	N configuration (at%)				O configuration (at%)			S configuration (at%)			
Samples	N-6	N-5	N-Q	N-X	O-I	O-II	O-III	S1	S2	S3	Specific capacitance (F g^{-1})
NOSC-800	21.04	27.93	47.95	3.08	30.97	35.25	33.78	57.88	28.91	13.21	84.20
NOSPC-700	41.62	24.21	18.32	15.86	25.40	31.57	43.03	45.05	40.59	14.36	236.72
NOSPC-800	59.66	17.70	11.05	11.59	20.48	47.11	32.40	58.07	17.14	24.79	324.06
NOSPC-900	50.90	19.23	12.95	16.91	34.21	37.51	28.28	66.29	32.05	1.66	265.04

Open Access Article. Published on 13 November 2020. Downloaded on 2/25/2026 10:59:45 AM.
This article is licensed under a Creative Commons Attribution-NonCommercial 3.0 Unported Licence.

reactions.[8,43] Furthermore, S1 can enhance the conductivity owing to delocalized electrons on the conjugated backbones of carbon, while S3 endows the high affinitive carbon matrix and provides a polarized surface and reversible pseudo-sites, as a result increases the capacitive performance.[26,42] The NOSPC-800 carbon sample, which shows the best electrochemical supercapacitor performance in this study, has a N-6 relative content up to 59.66%, an O-II relative content up to 47.11%, and the total content of S1 and S3 accounts for 82.86%, all of which are the highest among the carbon samples (Table 2). It is believed that the synergistic effect of the structural features of carbon materials, such as high SSA with a proper hierarchical structure, adequate N, O and S contents in a suitable chemical configuration distribution, make contributions together to the electrochemical performance of carbon-based supercapacitors.[11,44]

Electrocatalytic oxygen reduction reaction (ORR) performance

In addition to working as supercapacitor electrodes, the obtained carbons with promising structures and compositions are also expected to show potentiality in the electrocatalysis field. The electrocatalytic activity of NOSPC-800 and Pt/C catalysts was evaluated firstly by cyclic voltammetry measurements in 0.1 M KOH solution with N_2 or O_2 saturated. As shown in Fig. 8(a), there is an obvious characteristic reduction peak appeared at *ca.* −0.12 V of NOSPC-800 in the O_2 saturated alkaline electrolyte, compared with a rather smooth CV under N_2 condition, indicating that the apparent ORR occurred on the electrode in O_2 saturated electrolyte.[45] Although the oxygen reduction peak potential of NOSPC-800 (−0.12 V) is lower than that of Pt/C (0 V), the catalytic current is much higher, suggesting that NOSPC-800 has good electrocatalytic activity for ORR. LSV tests were carried out on the catalyst at different scanning rates using a rotating disk electrode, as shown in Fig. 8(b), in order to better investigate the ORR reaction kinetics of NOSPC-800. It can be seen clearly that the current density increases with the increase of rotating speed from 400 to 2500 rpm because of the shortened diffusion layer for electrode material, which indicates that the ORR is controlled and influenced by the diffusion rate.[46] Fig. 8(c) shows the K–L curves corresponding to the LSV test by rotating disk electrode (RDE), and it can be observed that the reciprocal of current density is linear with the reciprocal of rotating speed of turntable, which proves that the catalytic process conforms to the first-order reaction kinetics. The number of electron transfer of NOSPC-800 in the ORR reaction was calculated by K–L equation (Fig. 8(d)). The number of electron transfer was 3.1, 3.2, 3.7 and 4.0, corresponding to the potential of −0.5 V, −0.6 V, −0.7 V and −0.8 V, respectively, which indicates that the ORR reaction of NOSPC-800 conformed to the four electron transfer pathway.[47] The good electrocatalytic activities may be due to optimal pore size distribution and activated interfaces by introducing more active sites through N/S co-doping, which results in superior ORR activity of NOSPC-800.

Methanol toxicity resistance and long-term electrochemical stability of ORR catalysts are two critical indexes for actual applications. As shown in Fig. 9(a) and (b), the long-term catalytic performance stability of Pt/C and NOSPC-800 is compared through the accelerated durability testing (ADT). It can be found that both Pt/C and NOSPC-800 show gradual attenuation after 1000 CV cycles, while the current density of NOSPC-800 has a retention up to 99% of the initial current density, much higher than that of Pt/C (∼95%), indicating that NOSPC-800 has more stable catalytic activity than Pt/C. Fig. 9(c) and (d) show the methanol toxicity resistance of Pt/C and NOSPC-800 respectively. The RDE polarization curve of Pt/C shows a large oxidation peak at the potential of −0.18 V in the methanol containing electrolyte, indicating that the Pt/C electrode has poor methanol toxicity resistance. Compared with the obvious retardance of Pt/C, there is only negligible change of the RDE polarization curve of NOSPC-800 in methanol, which shows that NOSPC-800 has an excellent methanol toxicity resistance, which has potential applications in methanol fuel cells. Moreover, NOSPC-800 shows half-wave potential of −0.12 V and the largest current

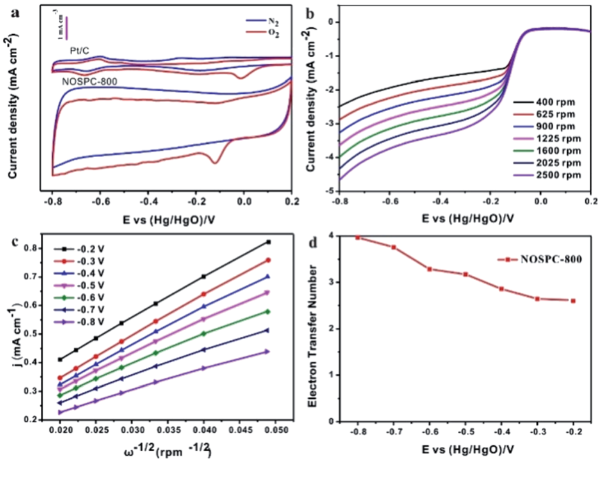

Fig. 8 (a) CV curves of Pt/C and NOSPC-800 in N_2 and O_2 saturated 0.1 M KOH electrolyte at 50 mV s^{-1}; (b) LSVs of oxygen reduction on NOSPC-800 at various rotation speeds; (c) corresponding K–L plots of NOSPC-800; (d) the electron transfer numbers of NOSPC-800.

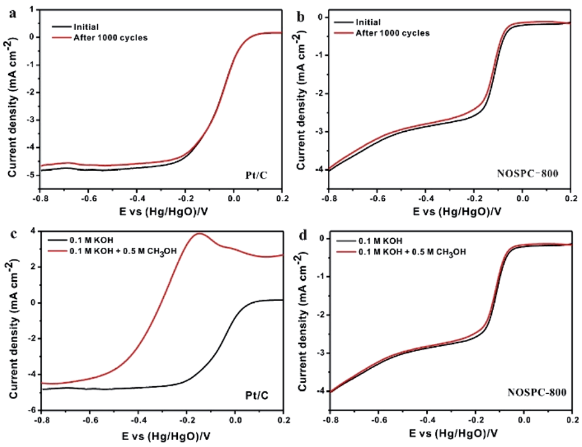

Fig. 9 LSV curves of the initial and after 1000 CV cycles for (a) Pt/C and (b) NOSPC-800; LSV curves of the initial and after 1000 CV cycles of methanol toxicity test for (c) Pt/C and (d) NOSPC-800.

Open Access Article. Published on 13 November 2020. Downloaded on 2/25/2026 10:59:45 AM. This article is licensed under a Creative Commons Attribution-NonCommercial 3.0 Unported Licence.

density of 4.09 mA cm^{-2} at -0.8 V, both of which are quite close to and only slightly lower than those of commercial Pt/C (-0.07 V, 5.09 mA cm^{-2}), indicative of a higher density of surface-active sites as well as outstanding ORR performance.

Conclusions

In summary, we present a facile and efficient preparation method of N/S co-doped hierarchical porous carbon from organic waste (Chinese gallnut residues) without any extra heteroatom materials source, *via* carbonization and subsequent KOH activation. The prepared NOSPC-*X* carbon materials show high specific surface areas, abundant micro-/meso-porous structures, and with high N/S co-doping content. The NOSPC-800 carbon material is found to show both good supercapacitor performance and ORR activity. The unique features of the composition and structure endow the carbon material an outstanding electrode material for supercapacitor with a high specific capacitance in a two-electrode system, good capacitance retention capability (70% retention at current densities up to 20 A g^{-1}) and good cycling stability (96.5% retention of the initial specific capacitance after 10 000 cycles). The material also exhibits excellent electrocatalytic properties for oxygen reduction reaction. NOSPC-800 shows a more positive half-wave potential, and it also has a large current density (4.09 mA cm^{-2} at 0.8 V) which is very close to that of commercial Pt/C electrocatalyst. Furthermore, it also exhibits superior stability and better resistance to methanol than commercial Pt/C catalyst. These results demonstrate that biomass-derived NOSPC-800 is a promising candidate as an excellent electrode material in the prospective industrial applications. Our study provides an *in situ* and effective heteroatoms co-doping method in the controllable construction of hierarchical porous carbon materials, as well as a new path of high value utilization of Chinese herbal residues.

Conflicts of interest

There are no conflicts to declare.

Acknowledgements

The authors are grateful for the financial support from Guizhou Science and Technology Program Project No. [2017]1024, Guizhou Science and Technology Cooperation Platform Talents Program No. [2018]5781, Science and Technology Department of Guizhou Province (Grant No. Platform & Talents [2016]5652; [2019]5607).

Notes and references

1 A. Muzaffar, M. B. Ahamed, K. Deshmukh and J. Thirumalai, *Renew. Sustain. Energy Rev.*, 2019, **101**, 123–145.
2 L. Du, L. X. Xing, G. X. Zhang and S. H. Sun, *Carbon*, 2020, **156**, 77–92.
3 N. Choudhary, C. Li, J. Moore, N. Nagaiah, L. Zhai, Y. Jung and J. Thomas, *Adv. Mater.*, 2017, **29**, 30.
4 B. Wang, T. T. Ruan, Y. Chen, F. Jin, L. Peng, Y. Zhou, D. L. Wang and S. X. Dou, *Energy Storage Mater.*, 2020, **24**, 22–51.
5 J. G. Wang, H. Z. Liu, H. H. Sun, W. Hua, H. W. Wang, X. R. Liu and B. Q. Wei, *Carbon*, 2018, **127**, 85–92.
6 H. Jiang, J. X. Gu, X. S. Zheng, M. Liu, X. Q. Qiu, L. B. Wang, W. Z. Li, Z. F. Chen, X. B. Ji and J. Li, *Energy Environ. Sci.*, 2019, **12**, 322–333.
7 M. H. Shao, Q. W. Chang, J. P. Dodelet and R. Chenitz, *Chem. Rev.*, 2016, **116**, 3594–3657.
8 Z. Song, D. Zhu, L. Li, T. Chen, H. Duan, Z. Wang, Y. Lv, W. Xiong, M. Liu and L. Gan, *J. Mater. Chem. A*, 2019, **7**, 1177–1186.
9 W. Yang, W. Yang, L. N. Kong, A. L. Song, X. J. Qin and G. J. Shao, *Carbon*, 2018, **127**, 557–567.
10 T. Y. Liu, F. Zhang, Y. Song and Y. Li, *J. Mater. Chem. A*, 2017, **5**, 17705–17733.
11 H. B. Feng, H. Hu, H. W. Dong, Y. Xiao, Y. J. Cai, B. F. Lei, Y. L. Liu and M. T. Zheng, *J. Power Sources*, 2016, **302**, 164–173.
12 S. Y. Gao, L. Y. Li, K. R. Geng, X. J. Wei and S. X. Zhang, *Nano Energy*, 2015, **16**, 408–418.
13 Z. J. Tang, Z. X. Pei, Z. F. Wang, H. F. Li, J. Zeng, Z. H. Ruan, Y. Huang, M. S. Zhu, Q. Xue, J. Yu and C. Y. Zhi, *Carbon*, 2018, **130**, 532–543.
14 A. K. Mondal, K. Kretschmer, Y. F. Zhao, H. Liu, C. Y. Wang, B. Sun and G. X. Wang, *Chem.–Eur. J.*, 2017, **23**, 3683–3690.
15 S. Xiong, J. Fan, Y. Wang, J. Zhu, J. Yu and Z. Hu, *J. Mater. Chem. A*, 2017, **5**, 18242–18252.
16 S. Gao, X. Li, L. Li and X. Wei, *Nano Energy*, 2017, **33**, 334–342.
17 L. J. Yang, J. L. Shui, L. Du, Y. Y. Shao, J. Liu, L. M. Dai and Z. Hu, *Adv. Mater.*, 2019, **31**, 20.
18 L. L. Chen, X. L. Xu, W. X. Yang and J. B. Jia, *Chin. Chem. Lett.*, 2020, **31**, 626–634.
19 S. L. Zhao, X. Y. Lu, L. Z. Wang, J. Gale and R. Amal, *Adv. Mater.*, 2019, **31**, 9.
20 A. B. Fuertes, G. A. Ferrero and M. Sevilla, *J. Mater. Chem. A*, 2014, **2**, 14439–14448.
21 Q. Zhang, K. H. Han, S. J. Li, M. Li, J. X. Li and K. Ren, *Nanoscale*, 2018, **10**, 2427–2437.
22 H. G. Wei, H. Wang, A. Li, H. Q. Li, D. P. Cui, M. Y. Dong, J. Lin, J. C. Fan, J. X. Zhang, H. Hou, Y. P. Shi, D. F. Zhou and Z. H. Guo, *J. Alloys Compd.*, 2020, **820**, 10.
23 G. Y. Zhao, C. Chen, D. F. Yu, L. Sun, C. H. Yang, H. Zhang, Y. Sun, F. Besenbacher and M. Yu, *Nano Energy*, 2018, **47**, 547–555.
24 Y. N. Gong, D. L. Li, C. Z. Luo, Q. Fu and C. X. Pan, *Green Chem.*, 2017, **19**, 4132–4140.
25 B. Liu, Y. J. Liu, H. B. Chen, M. Yang and H. M. Li, *J. Power Sources*, 2017, **341**, 309–317.
26 L. Miao, D. Z. Zhu, M. X. Liu, H. Duan, Z. W. Wang, Y. K. Lv, W. Xiong, Q. J. Zhu, L. C. Li, X. L. Chai and L. H. Gan, *Chem. Eng. J.*, 2018, **347**, 233–242.
27 H. Lu and X. S. Zhao, *Sustainable Energy Fuels*, 2017, **1**, 1265–1281.

Open Access Article. Published on 13 November 2020. Downloaded on 2/25/2026 10:59:45 AM.
This article is licensed under a Creative Commons Attribution-NonCommercial 3.0 Unported Licence.

28 Q. H. Li, W. X. Chen, H. Xiao, Y. Gong, Z. Li, L. R. Zheng, X. S. Zheng, W. S. Yan, W. C. Cheong, R. A. Shen, N. H. Fu, L. Gu, Z. B. Zhuang, C. Chen, D. S. Wang, Q. Peng, J. Li and Y. D. Li, *Adv. Mater.*, 2018, **30**, 6.

29 L. Zhang, X. Hu, Z. Wang, F. Sun and D. G. Dorrell, *Renewable Sustainable Energy Rev.*, 2018, **81**, 1868–1878.

30 Q. Yuan, W. D. Li, Y. P. Zheng, J. Jin and S. Li, *Chin. J. Bioprocess Eng.*, 2019, **17**, 171–176.

31 B. Yang, F. Ding, W. D. Li, J. J. Jin, R. Tian, B. C. Cai and K. M. Qin, *Chin. Tradit. Herb. Drugs*, 2017, **48**(2), 377–383.

32 B. Li, F. Dai, Q. F. Xiao, L. Yang, J. M. Shen, C. M. Zhang and M. Cai, *Energy Environ. Sci.*, 2016, **9**, 102–106.

33 Z. Song, L. Li, D. Zhu, L. Miao, H. Duan, Z. Wang, W. Xiong, Y. Lv, M. Liu and L. Gan, *J. Mater. Chem. A*, 2019, **7**, 816–826.

34 X. J. Zheng, J. Wu, X. C. Cao, J. Abbott, C. Jin, H. B. Wang, P. Strasser, R. Z. Yang, X. Chen and G. Wu, *Appl. Catal., B*, 2019, **241**, 442–451.

35 M. Sun, D. Davenport, H. J. Liu, J. H. Qu, M. Elimelech and J. H. Li, *J. Mater. Chem. A*, 2018, **6**, 2527–2539.

36 M. Borghei, J. Lehtonen, L. Liu and O. J. Rojas, *Adv. Mater.*, 2018, **30**, 27.

37 A. Sarapuu, E. Kibena-Poldsepp, M. Borghei and K. Tammeveski, *J. Mater. Chem. A*, 2018, **6**, 776–804.

38 J. Z. Chen, J. L. Xu, S. Zhou, N. Zhao and C. P. Wong, *Nano Energy*, 2016, **25**, 193–202.

39 J. Yang, F. Xiang, H. Guo, L. P. Wang and X. B. Niu, *Carbon*, 2020, **156**, 514–522.

40 J. J. He, D. Y. Zhang, Y. L. Wang, J. W. Zhang, B. B. Yang, H. Shi, K. J. Wang and Y. Wang, *Appl. Surf. Sci.*, 2020, **515**, 12.

41 J. Pang, W. F. Zhang, J. L. Zhang, G. P. Cao, M. F. Han and Y. S. Yang, *Green Chem.*, 2017, **19**, 3916–3926.

42 L. Miao, H. Duan, M. X. Liu, W. J. Lu, D. Z. Zhu, T. Chen, L. C. Li and L. H. Gan, *Chem. Eng. J.*, 2017, **317**, 651–659.

43 D. F. Xue, D. Z. Zhu, W. Xiong, T. C. Cao, Z. W. Wang, Y. K. Lv, L. C. Li, M. X. Liu and L. H. Gan, *ACS Sustain. Chem. Eng.*, 2019, **7**, 7024–7034.

44 H. Wang, W. Zhang, P. Bai and L. Xu, *Ultrason. Sonochem.*, 2020, **65**, 105048.

45 G. X. Lin, R. G. Ma, Y. Zhou, Q. Liu, X. P. Dong and J. C. Wang, *Electrochim. Acta*, 2018, **261**, 49–57.

46 B. B. Guo, R. G. Ma, Z. C. Li, S. K. Guo, J. Luo, M. H. Yang, Q. Liu, T. Thomas and J. C. Wang, *Nano-Micro Lett.*, 2020, **12**, 13.

47 X. X. Huang, T. Shen, T. Zhang, H. L. Qiu, X. X. Gu, Z. Ali and Y. L. Hou, *Adv. Energy Mater.*, 2020, **10**, 21.